RESEARCH

A Highly Frequency-Selective 3D-Printed Dielectric Structure for the Terahertz Range

Tobias Kubiczek[1] · Kevin Kolpatzeck[1] · Thorsten Schultze[1] · Jan C. Balzer[1]

Abstract

In this paper, we present a terahertz transmission frequency-selective quasi surface (FSQS) that exhibits strong absorption lines and a periodic band-pass characteristic. The FSQS structure is created by laterally combining Fabry-Pérot resonators with different thicknesses. The transfer function of the FSQS can serve as a broadband reference for testing the signal integrity of the transmission path for broadband terahertz systems. The transfer function achieves a combination of band-pass characteristics and sharp resonances with a theoretical attenuation of over 80 dB and with quality factors of more than 40,000 for a combination of 36 resonators. A single FSQS made up of four resonators is 3D printed by fused deposition modeling using a low-loss cyclic olefin copolymer (COC) filament. Finally, the 3D-printed FSQS is characterized using both frequency-domain and time-domain terahertz spectroscopy. The results show an attenuation of over 42 dB and a quality factor above 100.

✉ Tobias Kubiczek
tobias.kubiczek@uni-due.de

Kevin Kolpatzeck
kevin.kolpatzeck@uni-due.de

Thorsten Schultze
thorsten.schultze@uni-due.de

Jan C. Balzer
jan.balzer@uni-due.de

1 Chair of Communication Systems, University of Duisburg-Essen, Bismarckstr. 81, 47057 Dusiburg, Germany

1 Introduction

The bandwidth of terahertz spectrometers nowadays exceeds more than 10 THz with a dynamic range of more than 130 dB [1–3]. Possible applications include materials characterization [4], security applications [5], industrial non-destructive testing [6], and high-resolution 3D reconstruction of objects [7]. Most systems use a mechanical delay line or methods such as asynchronous optical sampling (ASOPS) [8, 9] or electronically controlled optical sampling (ECOPS) [10] for terahertz detection. A central problem is the occurrence of sampling errors that lead to artifacts in the recorded terahertz spectra [11, 12]. To increase the usable bandwidth and to eliminate sampling artifacts, algorithms and methods for the correction of sampling errors are used [11–14]. However, the raw and corrected terahertz spectra must be verified.

In addition, the characteristics of the used terahertz system and the characteristics of the free space path also play an important role. To collimate or focus the terahertz radiation onto a sample, transmission paths with parabolic mirrors or dielectric lenses are often used. The frequency-dependent beam profile of the antennas and the properties of the used terahertz optics used make it difficult to achieve a perfectly aligned beam path over the entire frequency range [15, 16].

To test the integrity of the signal along with the path characteristics, an object with a well-known transfer function can be measured. A simple object such as a plane-parallel dielectric plate can be used to obtain a well-defined transfer function. This plate acts as a Fabry-Pérot (FP) resonator with a characteristically oscillating transfer function. However, the attenuation of the resonator in the stop-band does not exceed a few dB and has no sharp features. In this work, we present a structure with a more pronounced frequency response. A prototype of this structure was first presented by us in [17].

The structure consists of a combination of two or more FP resonators forming a laterally periodic structure. This frequency-selective quasi surface (FSQS) shows a theoretical stop-band attenuation of more than 50 dB for four and more than 80 dB for nine FP resonators, according to the analytically calculated transfer function. The corresponding Q factors are over 200 and over 40,000, respectively. The simplicity of the structure allows manufacturing by 3D printing techniques. The material used for manufacturing is cyclic olefin copolymer (COC), which shows an excellently low absorption that increases linearly to $1\,cm^{-1}$ at 2.6 THz and exhibits excellent printability in an fused deposition modeling (FDM) printing process [18–21]. Finally, an FSQS is fabricated and measured with two different terahertz spectrometers.

In Section 2, the design of the FSQS and the analysis of the theoretical transfer function are introduced. In Section 3, a manufactured and measured FSQS is presented, and the effects of alignment and inclined incidence are discussed. In Section 3, a summary is given.

2 Filter Design and Fabrication

By combining multiple FP resonators with different thicknesses, their sinusoidal transfer functions interfere. The resulting filter structure has a highly characteristic

transmission behavior. In this section, the analytical description of a single FP resonator is given. The model is then extended to multiple FP resonators. In the last part, the fabrication by 3D printing is discussed.

2.1 Single Fabry-Pérot Resonator

When electromagnetic radiation passes through a dielectric slab, it is split up into a reflected wave and a transmitted wave at each interface where a change of the refractive index occurs. This is illustrated in Fig. 1, where the incident wave $E_0(\omega)$ is directed at normal incidence onto a dielectric slab with the refractive index n_2 and the thickness d. The surrounding material is assumed to be air with a refractive index of $n_1 \approx 1.00027$ [22].

The ratios of the amplitudes of the reflected and transmitted wave to the incident wave are described by the Fresnel coefficients. For the calculation of the transmitted radiation, the transmission coefficients T_{12} and T_{21} as well as the reflection coefficient R_{21} for reflections within the material are of importance. For normal incidence and low material losses, the reflection coefficient is

$$R_{12} = \frac{n_1 - n_2}{n_1 + n_2} \tag{1}$$

for an interface between material 1 and material 2. The transmission coefficient from material 1 to material 2 is

$$T_{12} = \frac{2n_1}{n_1 + n_2}. \tag{2}$$

The transmitted wave through a dielectric sample is described as follows [23]:

$$E_t(\omega, d, n_1, n_2) = E_0(\omega) \cdot T_{12} \cdot P_2(\omega, d) \cdot T_{21} \cdot \sum_{u=0}^{k} \left[R_{21} \cdot P_2^2(\omega, d) \cdot R_{21} \right]^u, \tag{3}$$

Fig. 1 Transmitted wave $E_t(\omega)$ and reflected wave $E_r(\omega)$ at a dielectric material with the thickness d and the refractive index n_2 for the incoming wave $E_0(\omega)$. The material is surrounded by air with the refractive index $n_1 \approx 1.00027$
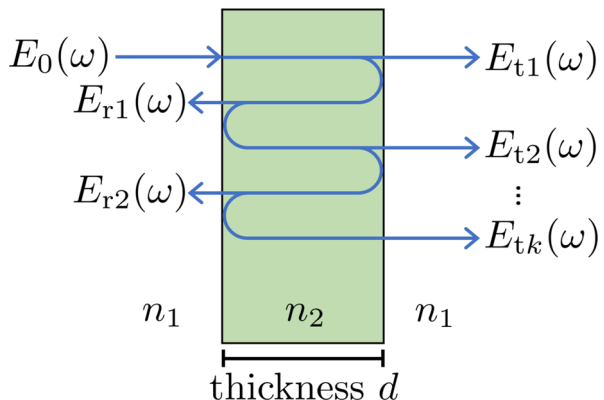
where

$$P_i(\omega, d) = \exp\left[-j\frac{n_i(\omega)\omega d}{c_0} - \frac{\alpha_i(\omega)d}{2}\right] \tag{4}$$

is the propagation term of material i over the distance d at the speed of light in vacuum c_0. α_i is the frequency-dependent absorption coefficient of material i. k is the number of reflections in the slab to be taken into account.

The visualization of the transfer function $\frac{E_t(\omega)}{E_0(\omega)}$ leads to the curves shown in Fig. 2. The visualization is for the material COC with the refractive index $n = 1.52$ (average of [19] and [20]) and the thicknesses $d = 1$ mm and $d = 1.5$ mm, respectively. The material losses are neglected.

Figure 2 shows that the attenuation of the transfer function of a single lossless FP resonator does not exceed 0.74 dB while introducing a constant phase slope. It can also be seen that the oscillation frequency is inversely proportional to the thickness of the FP resonator.

2.2 Multiple FP Resonators as a Frequency-Selective Quasi Surface

To increase the attenuation and obtain sharper spectral features, the interference between multiple FP resonators can be exploited. Combining multiple FP resonators of different thicknesses side by side results in the addition of different time delays and hence different oscillating transfer functions. The interference pattern depends strongly on the individual thicknesses of the resonators. A possible resonator design is presented in Fig. 3.

A 2×2 unit cell configuration is exemplary shown in Fig. 3a. To cover a desired area, each unit cell is repeated several times, as shown in Fig. 3b. The height of each
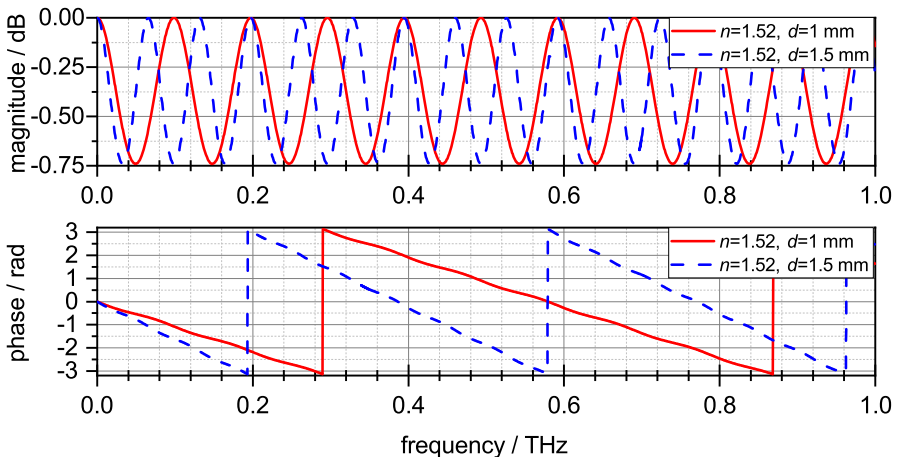

Fig. 2 The calculated transfer functions as magnitude and phase spectrum for Fabry-Pérot resonators made of COC with the refractive index of $n = 1.52$ and the thicknesses $d = 1$ mm and $d = 1.5$ mm, respectively. The attenuation for a single lossless FP resonator does not exceed 0.74 dB, and the oscillation frequency is anti-proportional to the thickness of the FP resonator
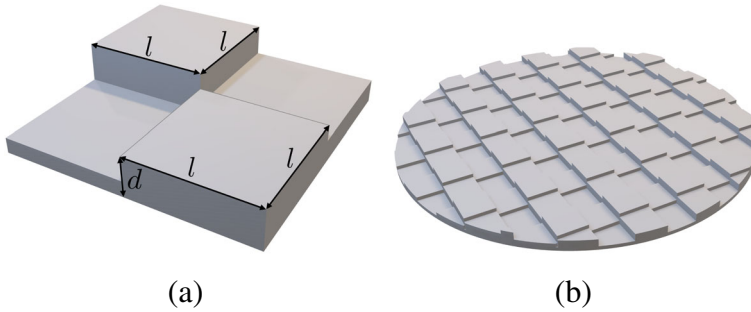
Fig. 3 Structure of the resonator including **a** the unit cell and **b** a 2-inch resonator structure where the unit cell is repeated over a disk. The square area of each FP resonator has the width l. The height of each individual resonator is d_n

individual resonator can be chosen to meet the desired transfer function requirements. Each resonator has a square base with the side length l and the height d. For a periodic structure, the height d is an integer multiple of the base height b with $d(m) = m \cdot b$. m ranges from 1 to the number of resonators N. The maximum number of resonators is limited by the resulting overall thickness and printability of the FSQS, as well as the realized surface area. Uniform illumination of the FSQS is required to achieve a well-defined frequency response.

The transfer function of the entire FSQS for normal incidence is calculated from the sum of the individual transfer functions of the FP resonators for all thicknesses with Eq. 3. To simplify the notation, the vector $\mathbf{d} = (d_1, d_1, \ldots, d_N)$ is defined to contain all the thicknesses used for the FSQS. The refractive index for the surrounding material air is $n_1 \approx 1.00027$.

The transmitted spectrum through the filter is given by

$$T(\omega, \mathbf{d}, n_1, n_2) = \frac{1}{N} \sum_{i=1}^{N} E_t(\omega, \mathbf{d}_i, n_1, n_2). \tag{5}$$

A visualization of possible transfer functions as magnitude and phase spectra can be seen in Fig. 4. The interference of multiple FP resonators results in periodic strong absorption lines. On the other hand, the transfer function shows periodic pass-band characteristics with low attenuation whose repetition frequency is proportional to the thickness b.

The attenuation between each pass-band is in the range of 11 dB for four resonators. For the combination of nine resonators, the attenuation increases to about 20 dB. The absorption lines at $f_1 = 1.5374$ THz and $f_2 = 1.7951$ THz show strong attenuations of 80.06 dB and 82.02 dB, respectively. The Q factors are 14,869 and 40,457, respectively. The combination of four resonators results in Q factors ranging from 157 at 289 GHz to 1146 at 1729 GHz.

Increasing the number of resonators highlights the potential of the FSQS to act as a transmission band-pass filter, as can be seen in Fig. 5.
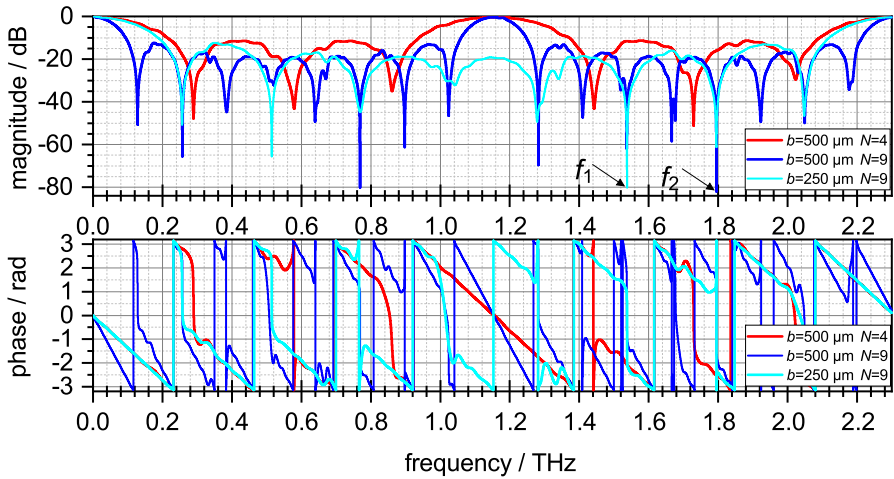
Fig. 4 Simulated transfer functions as magnitude and phase spectrum of FSQS designs with the parameters $b = 500\,\mu m$, $b = 250\,\mu m$ and varying N. As an example, the absorption lines at $f_1 = 1.5374$ THz and $f_2 = 1.7951$ THz show attenuations with 80.06 dB and 82.02 dB, and Q factors of 14,869 and 40,457, respectively

A higher number of FP resonators N results in a narrow main-lobe and an increased stop-band attenuation. Here, the combination of 36 resonators shows a 3 dB bandwidth of 41.54 GHz and a peak side lobe ratio of 13.12 dB. By changing the base height b, the target frequency of the pass-bands can be changed, as shown in Fig. 6. For a fixed number of resonators ($N = 9$), the pass-band frequency is inversely proportional to the base thickness. The periodicity of the band-pass characteristic with respect to the thickness b can be described as

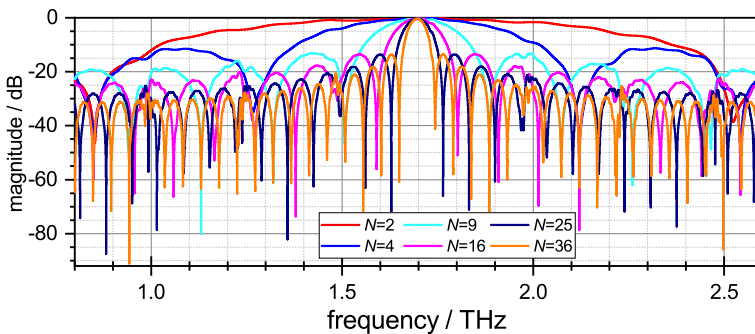$$f_{\text{band-pass}} = n \cdot \frac{c_0}{b(n_2 - n_1)}, \tag{6}$$

Fig. 5 Magnitude spectrum of the transfer functions for simulated resonator designs with $b = 340\,\mu m$ and a varying number of resonators N showing a narrowing main-lobe along with an increasing stop-band attenuation
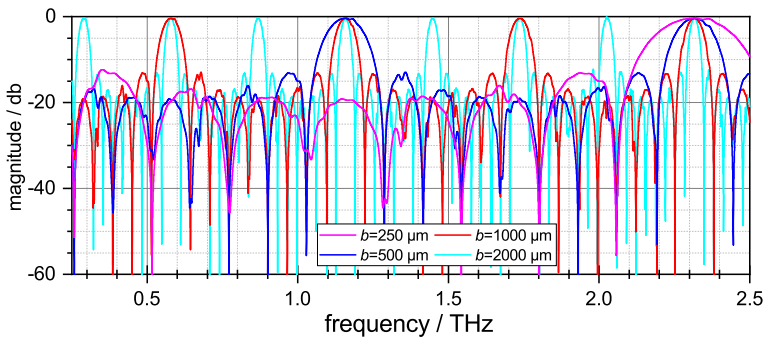
Fig. 6 Magnitude spectrum of the transfer functions for simulated resonator designs with $N = 9$ and a varying number of thicknesses b showing a the variation in the target frequency as well as the periodicity of the FSQS

where n is a positive integer multiple. Therewith, the spacing between the resonances Δf can be expressed by

$$\Delta f = \frac{1}{N} \cdot \frac{c_0}{b(n_2 - n_1)}. \tag{7}$$

2.3 Fabrication by 3D Printing

The simple 2.5-dimensional structure of the FSQS allows it to be manufactured using 3D printing techniques. The manufacturing is done by fused deposition modeling (FDM) 3D printing with the material COC. The low broadband absorption of COC, also known as TOPAS, in the terahertz region enables the manufacturing of high-quality transmission devices such as terahertz optics, waveguides, and filters [18–21].

Here, the Ultimaker S5 3D printer is used with a 0.23-mm diameter nozzle. The layer height is set to 100 µm. A printed FSQS with a 2×2 unit cell configuration is shown in Fig. 7. It is designed to fit into a 2-inch sample holder.
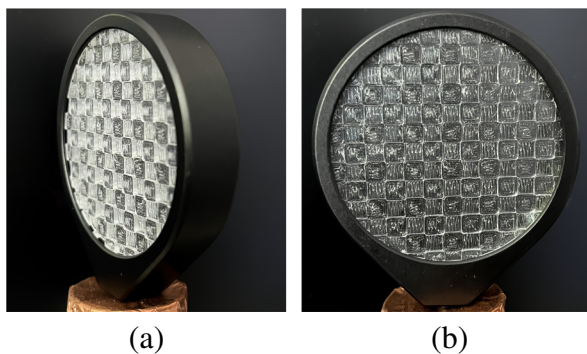

(a)   (b)

Fig. 7 3D-printed FSQS from a 2×2 unit cell configuration in **a** perspective view and **b** front view. The used material for manufacturing is COC

3 Results

To verify the theoretically calculated transfer function, measurements with two different terahertz spectrometers are performed on the 3D-printed 2×2 FSQS.

3.1 Experimental Setup

The terahertz time-domain spectroscopy (THz-TDS) system TeraK15 from Menlo Systems is used. It has a maximum bandwidth of about 6 THz with a maximum frequency resolution of 0.588 GHz. A sufficient dynamic range is typically achieved for frequencies above 250 GHz, and the peak dynamic range is reached at 1 THz. The terahertz frequency-domain spectroscopy (THz-FDS) system TeraScan 1550 from Toptica Photonics is used as a second measurement system. It has a bandwidth of 1.3 THz with a frequency resolution of 10 MHz. Both spectrometers are operated in a collimated transmission setup.

The THz-TDS system is operated with four lenses (4f configuration) as shown in Fig. 8. The THz-FDS system is operated with two parabolic mirrors to collimate the terahertz radiation. The FSQS is placed in the collimated part of the transmission setup to measure the transmitted wave $E_t(\omega)$. The incident radiation $E_0(\omega)$ is measured without the sample in the transmission path as a reference measurement.

3.2 Material Parameters

Since the dielectric properties of the 3D-printed COC filament are unknown and are important for a well-matching transfer function, an analysis of the dielectric properties is carried out. Therefore, a 2-mm thick slab of COC is 3D printed. The slab is measured with the previously described THz-TDS measurement setup, and additionally, a reference without the sample is also recorded.

By calculating the transfer function of the COC sample, the refractive index and the absorption coefficient of the material are calculated according to [4] and can be seen in Fig. 9. To minimize the influence of water absorption lines, the transfer function is transformed into the time domain and windowed, so that only the initial transmitted pulse is considered. The visible slight fluctuations are a direct effect of the window used. However, the introduced variations are less than 0.01% and are therefore well within the accuracy range achievable with a THz-TDS system [4].
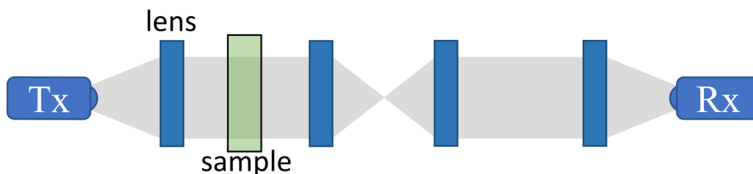

Fig. 8 Measurement setup in 4f configuration for collimated and focused transmission geometry. Lenses collimate and focus the emitted terahertz radiation and further refocus it onto the receiving antenna. The sample is placed in the collimated part of the setup
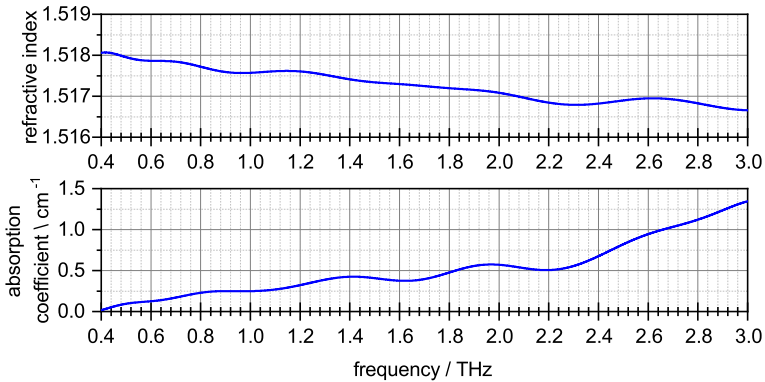
Fig. 9 Calculated refractive index *n* and absorption coefficient α from a 3D-printed slab of cyclic olefin copolymer which is measured in collimated transmission with a commercial terahertz time-domain spectrometer

The refractive index of the 3D-printed COC is close to 1.52 and decreases slightly at higher frequencies. In addition, the low losses highlight the importance of COC as a material for 3D-printed passive components in the terahertz range.

To further evaluate the influence of the frequency-dependent refractive index and absorption coefficient of the material, we compare the transfer function of a 2×2 FSQS calculated using ideal material parameters to that calculated using measured material parameters. On the one hand, the material parameters are kept constant with $n = 1.52$ and $\alpha = 0$. On the other hand, the measured material parameters are used.

The results are shown in Fig. 10. Both transfer functions are overall similar and show only small deviations, mainly visible at the resonances. In the pass-band section at 1.1 THz, an overall attenuation of 0.1 dB can be seen. At the resonance at 1.956 THz, the modeled transfer function for the measured material parameters shows 5 dB
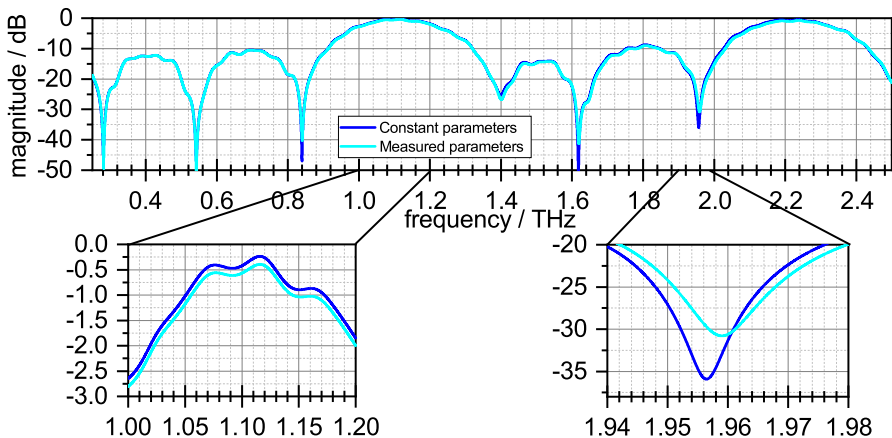

Fig. 10 Comparison of the simulated transfer function for a 2×2 FSQS modeled with a broadband constant refractive index $n = 1.52$ and absorption coefficient of 0 and measured material parameters

less attenuation and a slight shift of the resonance of 3 GHz. The resonance shift is a direct consequence of the slight change in the measured refractive index compared to the assumed constant refractive index. In a Fabry-Pérot resonator, a change in the refractive index causes a change in its resonance frequency. This has a direct effect on the resulting resonance frequencies of the combined structure.

3.3 Experimental Result

The first measurement is performed on an FSQS in 2×2 configuration with the parameters $b = 500\,\mu\text{m}$, $l = 2$ mm, and $N = 4$. The calculated transfer function as well as the measured transfer function $\frac{E_t(\omega)}{E_0(\omega)}$ can be seen in Fig. 11. Here, the measured thicknesses of each individual resonator were used to calculate the transfer function of the printed FSQS. Both measured transfer functions are similar and exhibit resonances at approximately the same frequencies. However, the slight variations in the resonances in the THz-TDS and THz-FDS measurements may be due to non-normal incidence of the terahertz waves in each individual path, as both systems use different optoelectronic terahertz transmitters and receivers. Even small changes in the incident angle can significantly shift the resonance frequencies.

A shift of the third and fourth resonance could also be caused by uncertainties in the 3D printing process combined with surface roughness. A measurement of the thickness of each resonator shows thicknesses of $460\,\mu\text{m}$, $999\,\mu\text{m}$, $1501\,\mu\text{m}$, and $2030\,\mu\text{m}$, respectively. This corresponds to thickness uncertainties of 8%, 0.1%, 0.1%, and 1.5%, respectively. The changes in the filter dimensions result in a detuning of the resonances.

The first resonance at $f_3 = 574$ GHz shows a quality factor of 78 for the THz-FDS measurement. The second resonance at $f_4 = 908$ GHz shows a quality factor of 105 for the THz-TDS measurement. The resonances are not clearly visible for low frequencies around 280 GHz in either measurement. This may be directly related to the chosen base width l which is 2 mm and corresponds to a wavelength of 150 GHz.
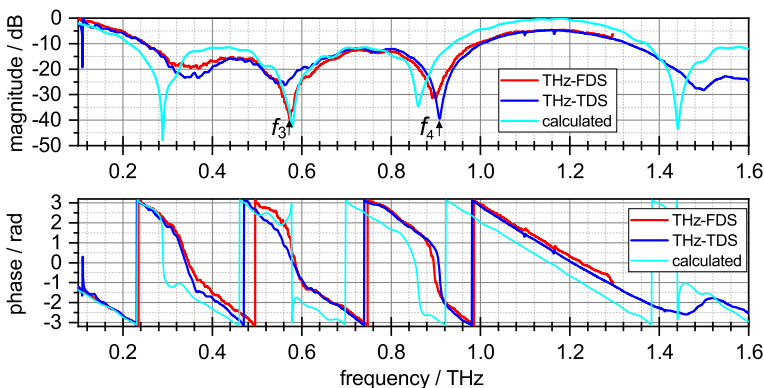

Fig. 11 Transfer function of the measured and modeled 2×2 FSQS design with the parameters $b = 500\,\mu\text{m}$, $l = 2$ mm, and $c = 4$. The calculated transfer function was calculated with the measured thicknesses

Grating effects at this wavelength can also be a problem. However, this problem can be solved by increasing the base size l for each resonator.

3.4 Effects of Alignment

To investigate the initial suspicion, that the alignment of the path and thus the angle of incidence to the FSQS plays an important role for the measured transfer function, a further measurement is performed with the THz-TDS system. For each measurement, the terahertz transmission path is realigned by removing and reinstalling all components. After each alignment, the 2×2 FSQS is measured accordingly with a reference.

The calculated transfer functions of the 2×2 FSQS for each alignment can be seen in Fig. 12. Remarkably, the pass-band attenuation at 1.15 THz and 2.3 THz varies by less than 1 dB. However, the resonances for all three alignments are not the same and show a visible shift. In addition, the quality factor for the resonances varies. This leads to the conclusion that the alignment of the used transmission setup has a direct influence on the measured transfer function of the FSQS. It is possible that the angle of incidence on the FSQS changes for different frequency components with each realignment. This leads to changed Fresnel coefficients and thus to different reflection and transmission behavior at the sample. Additionally, a changed incidence angle leads to a change of the physical resonator length.

3.5 Effects of Inclined Incidence

Since the angle of incidence seems to have an effect on the resonant frequencies, further investigations are carried out. For an inclined plane of incidence, the transmitted radiation shows a different behavior. Figure 13 visualizes the changed travel path through a dielectric slab. θ_i is the angle of incidence, and θ_t is the angle at which the radiation propagates through the slab.
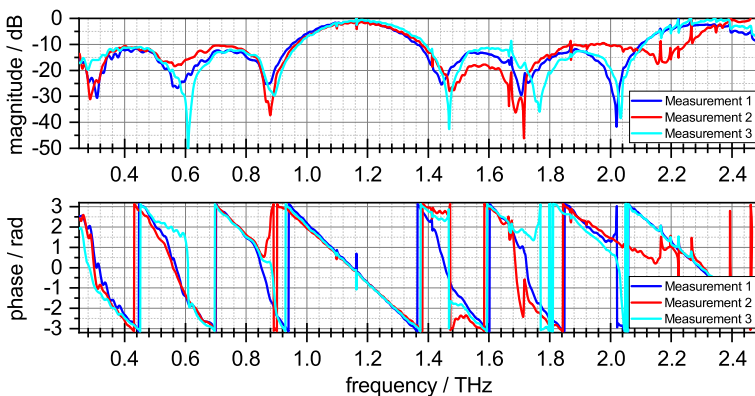

Fig. 12 Measured transfer function of a 2×2 FSQS with a realignment of the transmission path for each measurement. The THz-TDS system is used for the measurement
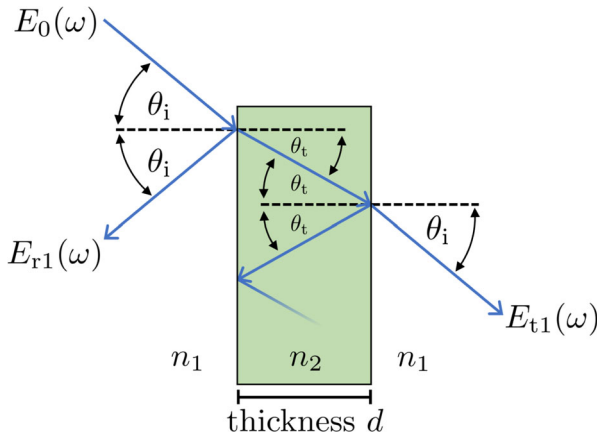
Fig. 13 Transmitted ($E_t(\omega)$) and reflected ($E_r(\omega)$) radiation at a dielectric slab with the thickness d and refractive index n_2 for an incoming radiation $E_0(\omega)$. The material is surrounded by air with the refractive index n_1. θ_i is the incidence angle, and θ_t is the angle at which the radiation propagates inside the slab

To investigate the rotational behavior of the filter, the setup of Fig. 8 is extended by a rotation stage, which is able to rotate the FSQS from -50 to $+50°$ and is further depicted in Fig. 14.

Now, a new 3D-printed FSQS is used with $l = 4$ mm, $b = 500$ μm, and $N = 4$. With an angular step size of $1°$, a terahertz trace is recorded at each step. The reference is recorded without a sample. In Fig. 15, the magnitude of the transfer function for each angle is visualized.

The resonance at low frequencies is directly noticeable, which contrasts with the previously measured transfer function. This can be explained by the increased effective width of the resonators l. Another notable feature is the change in resonance frequencies with inclined incidence. Specifically, the resonance at 680 GHz changes to 550 GHz with a $50°$ rotation. However, the effect of rotation on frequency change is stronger at higher frequencies. The resonance at 1.5 THz is detuned by 270 GHz to 1.23 THz when being rotated by $50°$. Additionally, a rotation of $1°$ results in a detuning of a few gigahertz. This measurement highlights the strong dependence of
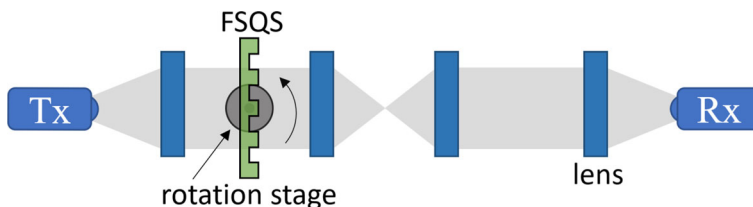

Fig. 14 Measurement setup in 4f configuration for collimated and focused transmission geometry. Lenses collimate and focus the emitted terahertz radiation and further refocus it onto the receiving antenna. The FSQS is placed in the collimated part of the setup and can be rotated by a rotation stage
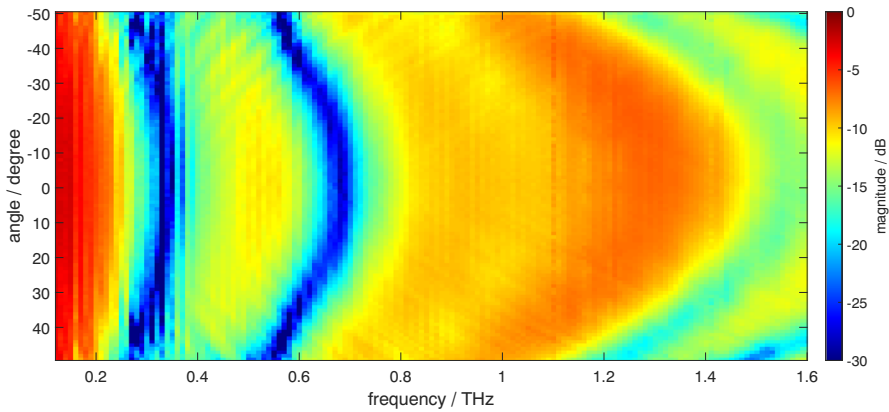
Fig. 15 Measured magnitude of the transfer function of the 2x2 FSQS design with the parameters $b = 500\,\mu m$, $l = 4$ mm, and $N = 4$. The FSQS was rotated from -50 to $+50°$

the measured transfer function of an FSQS on the alignment of the beam in the terahertz transmission setup. The frequency of the resonances is also highly sensitive to the incidence angle. If the theoretical transfer function and the measured transfer function of the FSQS are in good agreement, it can be assumed that the setup is well aligned.

4 Summary

In this paper, we have presented a broadband terahertz frequency-selective quasi surface that uses a combination of FP resonators with different thicknesses. The FSQS can be used to characterize the spectroscopic performance of terahertz systems. The characteristic interference pattern shows resonances with sharp absorption lines and a periodic band-pass characteristic. A 3D print of the FSQS was carried out using the low-absorptive material COC through FDM. The transfer function was calculated and verified through measurements using THz-TDS and THz-FDS. However, slight deviations were observed between the two measurement setups. The detuning of the resonances was likely caused by a shifted angle of incidence or by different beam profiles. A comparison of three alignments of a 4f transmission path showed that the structure gives a sensitive indication of deviations from a normal angle of incidence in a transmission setup. This structure can be used to evaluate the quality of a transmission path and identify issues with spectroscopic measurements of inhomogeneous samples using collimated beams. Therefore, after aligning a transmission setup, the measurement of an FSQS could identify non-idealities of the setup. Additionally, measuring at several angles could help determine the actual angle of incidence.

To improve the surface quality of the resonator, other 3D printing techniques like stereolithography 3D printing could be utilized. This technique would also allow for the use of resin materials and ceramics, which have a higher refractive index resulting in thinner resonators and a smaller filter design. One promising method is the 3D

printing of ceramics, which can achieve a resolution in the sub-100 μm range with low losses [24].

Data Availability No datasets were generated or analyzed during the current study.

Declarations

Ethics Approval Not applicable

Consent for Publication All the authors agreed to publish.

Conflict of Interest The authors declare no competing interests.

References

1. Kohlhaas, R.B., Breuer, S., Mutschall, S., Kehrt, M., Nellen, S., Liebermeister, L., Schell, M., Globisch, B.: Ultrabroadband terahertz time-domain spectroscopy using iii-v photoconductive membranes on silicon. Opt. Express. **30**(13), 23896–23908 (2022) https://doi.org/10.1364/OE.454447

2. Balzer, J.C., Saraceno, C.J., Koch, M., Kaurav, P., Pfeiffer, U.R., Withayachumnankul, W., Kürner, T., Stöhr, A., El-Absi, M., Abbas, A.A.-H., Kaiser, T., Czylwik, A.: Thz systems exploiting photonics and communications technologies. IEEE Journal of Microwaves. **3**(1), 268–288 (2023) https://doi.org/10.1109/JMW.2022.3228118

3. Cherniak, V., Kubiczek, T., Kolpatzeck, K., Balzer, J.C.: Laser diode based thz-tds system with 133 db peak signal-to-noise ratio at 100 ghz. Scientific Reports. **13**(1), 13476 (2023) https://doi.org/10.1038/s41598-023-40634-3

4. Jepsen, P.U., Cooke, D.G., Koch, M.: Terahertz spectroscopy and imaging – modern techniques and applications. Laser & Photonics Reviews **5**(1), 124–166 (2011) https://doi.org/10.1002/lpor.201000011. https://onlinelibrary.wiley.com/doi/pdf/10.1002/lpor.201000011

5. Naftaly, M., Vieweg, N., Deninger, A.: Industrial applications of terahertz sensing: State of play. Sensors. **19**(19) (2019) https://doi.org/10.3390/s19194203

6. Tao, Y.H., Fitzgerald, A.J., Wallace, V.P.: Non-contact, non-destructive testing in various industrial sectors with terahertz technology. Sensors. **20**(3) (2020) https://doi.org/10.3390/s20030712

7. Damyanov, D., Kubiczek, T., Kolpatzeck, K., Czylwik, A., Schultze, T., Balzer, J.C.: 3d thz-tds sar imaging by an inverse synthetic cylindrical aperture. IEEE Access. **11**, 9680–9690 (2023) https://doi.org/10.1109/ACCESS.2023.3240101

8. Janke, C., Först, M., Nagel, M., Kurz, H., Bartels, A.: Asynchronous optical sampling for high-speed characterization of integrated resonant terahertz sensors. Opt. Lett. **30**(11), 1405–1407 (2005) https://doi.org/10.1364/OL.30.001405

9. Yasui, T., Saneyoshi, E., Araki, T.: Asynchronous optical sampling terahertz time-domain spectroscopy for ultrahigh spectral resolution and rapid data acquisition. Applied Physics Letters. **87**(6), 061101 (2005) 1 https://doi.org/10.1063/1.2008379

10. Kim, Y., Yee, D.-S.: High-speed terahertz time-domain spectroscopy based on electronically controlled optical sampling. Opt. Lett. **35**(22), 3715–3717 (2010) https://doi.org/10.1364/OL.35.003715

11. Rehn, A., Jahn, D., Balzer, J.C., Koch, M.: Periodic sampling errors in terahertz time-domain measurements. Opt. Express. **25**(6), 6712–6724 (2017) https://doi.org/10.1364/OE.25.006712

12. Takagi, S., Takahashi, S., Takeya, K., Tripathi, S.R.: Influence of delay stage positioning error on signal-to-noise ratio, dynamic range, and bandwidth of terahertz time-domain spectroscopy. Appl. Opt. **59**(3), 841–845 (2020) https://doi.org/10.1364/AO.378756

13. Molter, D., Trierweiler, M., Ellrich, F., Jonuscheit, J., Freymann, G.V.: Interferometry-aided terahertz time-domain spectroscopy. Opt. Express. **25**(7), 7547–7558 (2017) https://doi.org/10.1364/OE.25.007547

14. Kolpatzeck, K., Liu, X., Häring, L., Balzer, J.C., Czylwik, A.: Ultra-high repetition rate terahertz time-domain spectroscopy for micrometer layer thickness measurement. Sensors. **21**(16) (2021) https://doi.org/10.3390/s21165389

15. Nellen, S., Lauck, S., Schwanke, G., Deumer, M., Kohlhaas, R.B., Liebermeister, L., Schell, M., Globisch, B.: Radiation pattern of planar optoelectronic antennas for broadband continuous-wave terahertz emission. Opt. Express. **29**(6), 8244–8257 (2021) https://doi.org/10.1364/OE.416844

16. Kolpatzeck, K., Liu, X., Friederich, B., Damyanov, D., Häring, L., Schultze, T., Balzer, J.C., Czylwik, A.: Wideband radiation pattern measurement of terahertz antenna-integrated photodiodes by frequency-domain spectroscopy. In: 2019 Second International Workshop on Mobile Terahertz Systems (IWMTS), pp. 1–5 (2019). https://doi.org/10.1109/IWMTS.2019.8823782

17. Kubiczek, T., Kolpatzeck, K., Schultze, T., Balzer, J.C.: 3d printed terahertz filter as a broadband frequency reference. In: 2022 47th International Conference on Infrared, Millimeter and Terahertz Waves (IRMMW-THz), pp. 1–2 (2022). https://doi.org/10.1109/IRMMW-THz50927.2022.9895494

18. Busch, S.F., Weidenbach, M., Balzer, J.C., Koch, M.: Thz optics 3d printed with topas. Journal of Infrared, Millimeter, and Terahertz Waves. **37**(25), 303–307 (2016) https://doi.org/10.1007/s10762-015-0236-7

19. Mavrona, E., Graf, J., Hack, E., Zolliker, P.: Optimized 3d printing of thz waveguides with cyclic olefin copolymer. Opt. Mater. Express. **11**(8), 2495–2504 (2021) https://doi.org/10.1364/OME.428378

20. Kubiczek, T., Balzer, J.C.: Material classification for terahertz images based on neural networks. IEEE Access. **10**, 88667–88677 (2022) https://doi.org/10.1109/ACCESS.2022.3200473

21. Kubiczek, T., Liu, X., Balzer, J.C., Guo, X., Sakaki, M., Zhao, Y., Benson, N.: 3d printed passive beam-guiding and manipulating devices for the terahertz frequency range. In: 2022 IEEE 12th International Conference on RFID Technology and Applications (RFID-TA), pp. 43–46 (2022). https://doi.org/10.1109/RFID-TA54958.2022.9923966

22. Mathar, R.J.: Refractive index of humid air in the infrared: model fits. Journal of Optics A: Pure and Applied Optics. **9**(5), 470 (2007) https://doi.org/10.1088/1464-4258/9/5/008

23. Duvillaret, L., Garet, F., Coutaz, J.-L.: A reliable method for extraction of material parameters in terahertz time-domain spectroscopy. IEEE Journal of Selected Topics in Quantum Electronics. **2**(3), 739–746 (1996) https://doi.org/10.1109/2944.571775

24. Ornik, J., Sakaki, M., Koch, M., Balzer, J.C., Benson, N.: 3d printed al2o3 for terahertz technology. IEEE Access. **9**, 5986–5993 (2021) https://doi.org/10.1109/ACCESS.2020.3047514